







Ionic contrast across a lipid membrane for Debye length extension: towards an ultimate bioelectronic transducer

Donggeun Lee ^{1,2,7}, Woo Hyuk Jung^{3,7}, Suho Lee⁴, Eui-Sang Yu ¹, Taikjin Lee¹, Jae Hun Kim¹, Hyun Seok Song¹, Kwan Hyi Lee ^{5,6}, Seok Lee¹, Sang-Kook Han², Myung Chul Choi⁴, Dong June Ahn ^{3,6,8}✉, Yong-Sang Ryu ^{1,6,8}✉ & Chulki Kim ^{1,8}✉

Despite technological advances in biomolecule detections, evaluation of molecular interactions via potentiometric devices under ion-enriched solutions has remained a long-standing problem. To avoid severe performance degradation of bioelectronics by ionic screening effects, we cover probe surfaces of field effect transistors with a single film of the supported lipid bilayer, and realize respectable potentiometric signals from receptor–ligand bindings irrespective of ionic strength of bulky solutions by placing an ion-free water layer underneath the supported lipid bilayer. High-energy X-ray reflectometry together with the circuit analysis and molecular dynamics simulation discovered biochemical findings that effective electrical signals dominantly originated from the sub-nanoscale conformational change of lipids in the course of receptor–ligand bindings. Beyond thorough analysis on the underlying mechanism at the molecular level, the proposed supported lipid bilayer–field effect transistor platform ensures the world-record level of sensitivity in molecular detection with excellent reproducibility regardless of molecular charges and environmental ionic conditions.

¹Sensor System Research Center, Korea Institute of Science and Technology, Seoul, Republic of Korea. ²Department of Electrical & Electronic Engineering, Yonsei University, Seoul, Republic of Korea. ³Department of Chemical and Biological Engineering, Korea University, Seoul, Republic of Korea. ⁴Department of Bio and Brain Engineering, Korea Advanced Institute of Science and Technology (KAIST), Daejeon, Republic of Korea. ⁵Center for Biomaterials, Korea Institute of Science and Technology, Seoul, Republic of Korea. ⁶KU-KIST Graduate School of Converging Science and Technology, Korea University, Seoul, Republic of Korea. ⁷These authors contributed equally: Donggeun Lee, Woo Hyuk Jung. ⁸These authors jointly supervised this work: Dong June Ahn, Yong-Sang Ryu, Chulki Kim. ✉email: ahn@korea.ac.kr; ysryu82@kist.re.kr; chulki.kim@kist.re.kr

Detection of molecular interactions between biomolecules and their counterparts, including antibody–antigen complexes^{1,2}, complementary single-stranded deoxyribonucleic acid^{3,4}, and enzyme–substrate interactions, has been demonstrated by various transducers with target-specific functionalization⁵. Detection of molecules via surface-sensitive bioelectronics has allowed for portable biomedical devices to implement point-of-care diagnostics to prescreen diseases without temporal and spatial limitations⁶. Among them, field-effect transistors (FETs) has attracted considerable attention because of their strength in miniaturization, cost-effective mass production, and seamless integration with manufacturing processes. Potential variations caused by molecular adsorption/desorption on the probing surface are effectively transduced into carrier density variation in the active current channel of FETs⁷, allowing “real-time” molecular detection without cumbersome labeling or signal-amplifying processes⁸. Despite the significant potential, molecular detection with FETs in ionic solutions at physiologic concentrations remains an ongoing challenge, mainly because of the formation of an “electrical double layer (EDL)” over the active sensing probe⁹ (Fig. 1a). Formation of the EDL originates from the fact that analytes electrically attract counter ions from an ionic solvent, causing exponential decay of electrical potential with distance. This screening effect inevitably limits the detection of induced potential variation arising from molecular interaction. For example, the effective detection range, termed Debye length (λ_D), becomes <1 nm in physiological conditions¹⁰. In addition, the non-specific binding of target molecules to the probe degrades sensor reliability by disrupting their selective sensing principles.

Thus, a novel strategy that can overcome the aforementioned hurdles is in high demand for unraveling the physicochemical nature of molecular interaction with biosensors.

Diverse efforts have been undertaken by facilitating advanced measurement scheme and functional materials such as heterodyne detection¹¹, antibody fragments¹², and deformable aptamers¹³, just to mention a few. Although these approaches shed light on molecular detection in ionic solutions, they still have certain limitations or require enhancements. The heterodyne detection, which results in complexity of the operating circuitry, was not functioned under physiological ionic strength conditions. Antibody fragments are placed on the probe surface with random orientations, which often degrades measurement reproducibility. Although deformable aptamers resolve previous shortcomings, aptamers require intensive work for their specific design. Along this line of thought, an ideal platform for biosensing applications is considered to, especially in physiological ionic strength conditions, be far from being established.

Here, we propose an ion-impermeable SLB-assisted FET (SLB-FET) platform for molecular detection with a high degree of consistency irrespective of environmental ionic conditions. The potential of supported lipid bilayers (SLBs), a mimicry of cellular membranes, as a bioelectronic transducer has been glimpsed¹⁴. Such a prospective conjecture in their biosensing applications originates from their nature: (i) high resistivity to non-specific protein adsorption¹⁵, (ii) surface passivation with ion impermeability¹⁴, and (iii) morphological preservation of receptors¹⁶. By turning the fascinating glimpse into the realization, we demonstrate robust molecular detection under biologically relevant conditions,

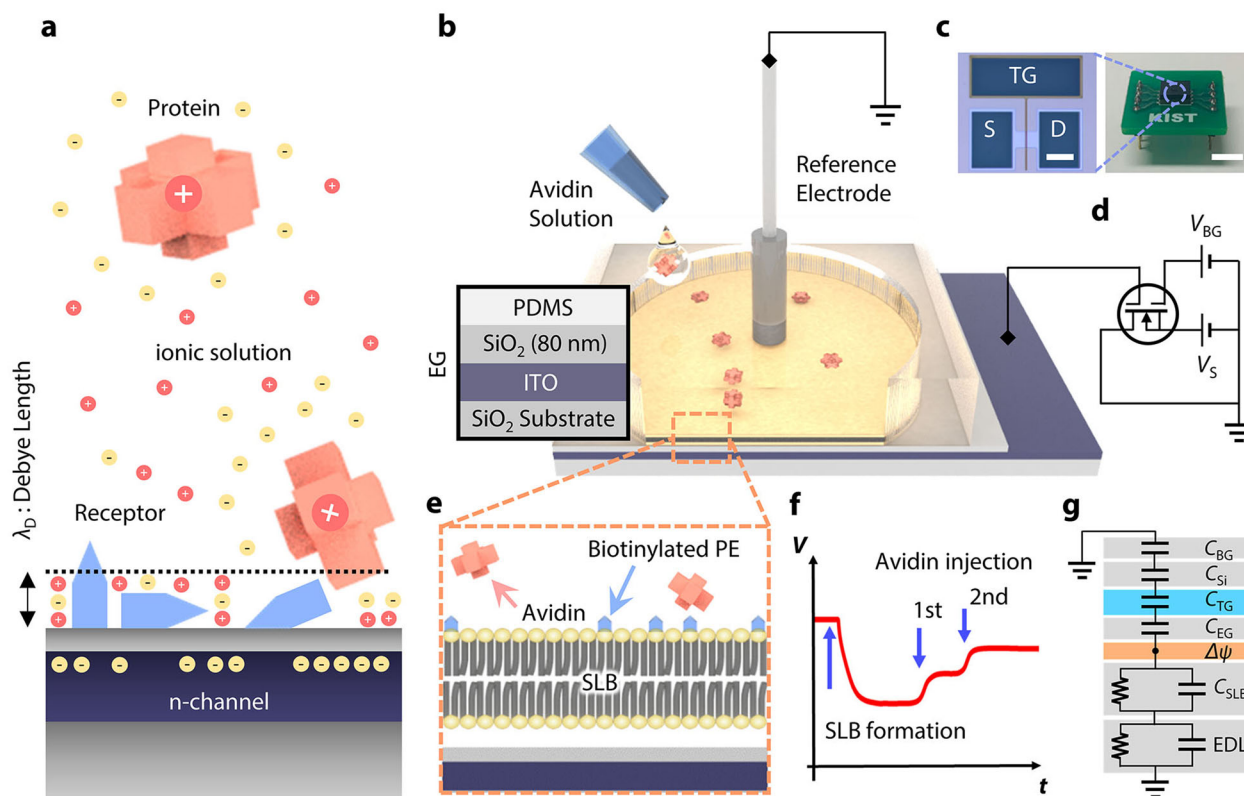


Fig. 1 Electrical sensing in ionic environments and schematic of the SLB-assisted FET measurement setup. **a** Challenges to potentiometric measurement schemes for molecular detection on an FET under ionic environment: formation of the EDL, non-specific binding, and randomly oriented receptors. **b** Schematic representation of a reaction chamber on the EG. (left) Layer-by-layer configuration of the EG. Polydimethylsiloxane (PDMS) chamber acts as a reaction chamber. **c** Optical images of the FET (left) and a packaged device (right) (scale bars = 100 μm and 5 mm, respectively). **d** Schematic representation of measurement setup. **e** Cross-sectional illustration of the SLB on the EG surface. **f** Proof-of-concept for real-time detection during biotin-avidin binding. **g** Equivalent circuit model for the measurement setup.

characterize its sensing capability in terms of sensitivity and selectivity, and finally investigate the signal transfer mechanism in our SLB-FET platform, which is triggered by real-time molecular bindings.

Result

Fabrication and measurement setup. The measurement setup for molecular detection comprises an FET and a reaction chamber placed on an extended gate (EG) (Fig. 1b, d). We fabricated FETs with an active channel in nanoscale by facilitating conventional semiconductor fabrication techniques (Fig. 1c and Supplementary Fig. 1). The thickness ratio of the top (14 nm) and bottom (750 nm) oxide layers determines its figure of merit¹⁷. The top gate electrode is electrically connected to an indium tin oxide (ITO) layer working as the EG electrode (see Supplementary Note 1 for details), wherein the gate potential change modulates the conductance in the FET. This allows for reliable data acquisition by eliminating any possible contamination or damage to the active channel of the FET. Furthermore, all the responses are transduced by an identical FET device, which enables direct comparison of individual signals measured with different analytes at various concentrations. To maximize the response amplitude, the back-gate voltage (V_{BG}) was adjusted to ensure the maximum slope in the top gate response curve (Supplementary Fig. 3).

Real-time monitoring of SLB coverage. SLB formation by spontaneous rupture of small unilamellar vesicles [SUV; $1 \mu\text{g mL}^{-1}$ in deionized water (DIW)] was examined using the FET (Fig. 2a). The SUV solution comprises 95% 1,2-dioleoyl-*sn*-glycero-3-phosphocholine (DOPC) and 5% 1,2-dioleoyl-*sn*-glycero-3-phosphoethanolamine-*N*-(cap biotinyl) (B-PE). Figure 2b shows the potential variation of the top gate electrode converted from the obtained current during the SLB formation (see “Methods” section for details). The observed saturation after the fourth injection of the SUV is consistent with the calculation that $0.4 \mu\text{g}$ of lipids is sufficient to completely cover the SiO_2 surface of the EG (see Supplementary Note 5 for details). An epifluorescence microscopy was

used for the cross-validation of the SLB formation (the inset of Fig. 2b).

Figure 2c shows drain current (I_D) as a function of V_{BG} with different SLB compositions, for direct comparison with compositional variations. The graph displays a signal resulting from the SLB containing 1 mol% of negatively charged Texas Red 1,2-dihexadecanoyl-*sn*-glycero-3-phosphoethanolamine (TR-DHPE)¹⁸ and shows a positive threshold voltage shift compared to the neutral SLB (DOPC 100%). Note that our SLB-FET platform demonstrates sufficient molecular sensitivity to distinguish compositional differences within the SLB. For a fluorescence recovery after the photobleaching (FRAP) test, we prepared a sample with the mol% ratio of 94:5:1 of DOPC:B-PE:TR-DHPE. The bleached region was recovered to 80% level of the initial fluorescent intensity after 10 min (Fig. 2d). With the lateral diffusion property of the lipids and the SLB with this compositional ratio, two effective binding sites of single avidin are assumed to be occupied avoiding steric hindrance¹⁹. The diffusion rate was calculated to be $1.43 \pm 0.4 \mu\text{m}^2 \text{s}^{-1}$ with high uniformity over the SiO_2 -coated EG^{20,21}.

Measurements of biotin-avidin bindings and analytical models.

To evaluate our SLB-FET as a biosensor operating in an ionic solution, we conducted time-lapse measurements during biotin-avidin binding. The SLB containing 5% of B-PE with 95% of DOPC was prepared on the EG surface¹⁹. After SLB deposition through SUV rupture in DIW, the outer buffer (OB) solution above the SLB was exchanged with $1\times$ phosphate buffer saline (PBS) to mimic physiologic conditions. Note that the ion impermeability of the SLB preserves the ionic imbalance across the lipid membrane (Supplementary Figs. 4 and 5). Figure 3a shows a typical real-time trace obtained from sequential steps including SLB formation (markers 1 and 2), OB exchange from DIW into $1\times$ PBS (marker 3), 800 pM-avidin injections (markers 4, 6, and 8), and 800 pM-Cholera toxin subunit B (CTxB) injections (markers 5 and 7). CTxB was applied as a negative control analyte. While CTxB injections showed no response, avidin injections led to clear changes of the top gate voltage ($\Delta V_{TG} \sim 4.7 \text{ mV}$ in the first injection) (Fig. 3b).

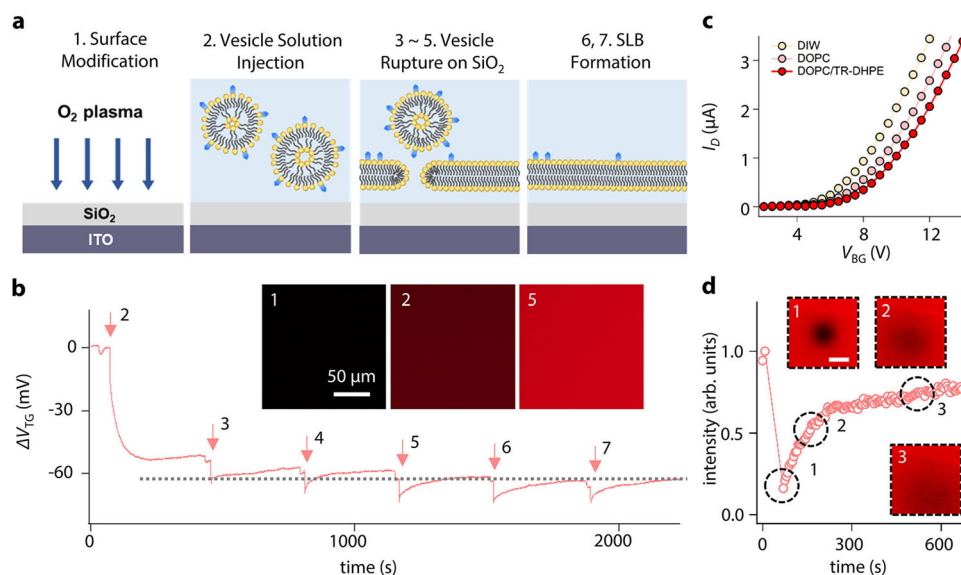
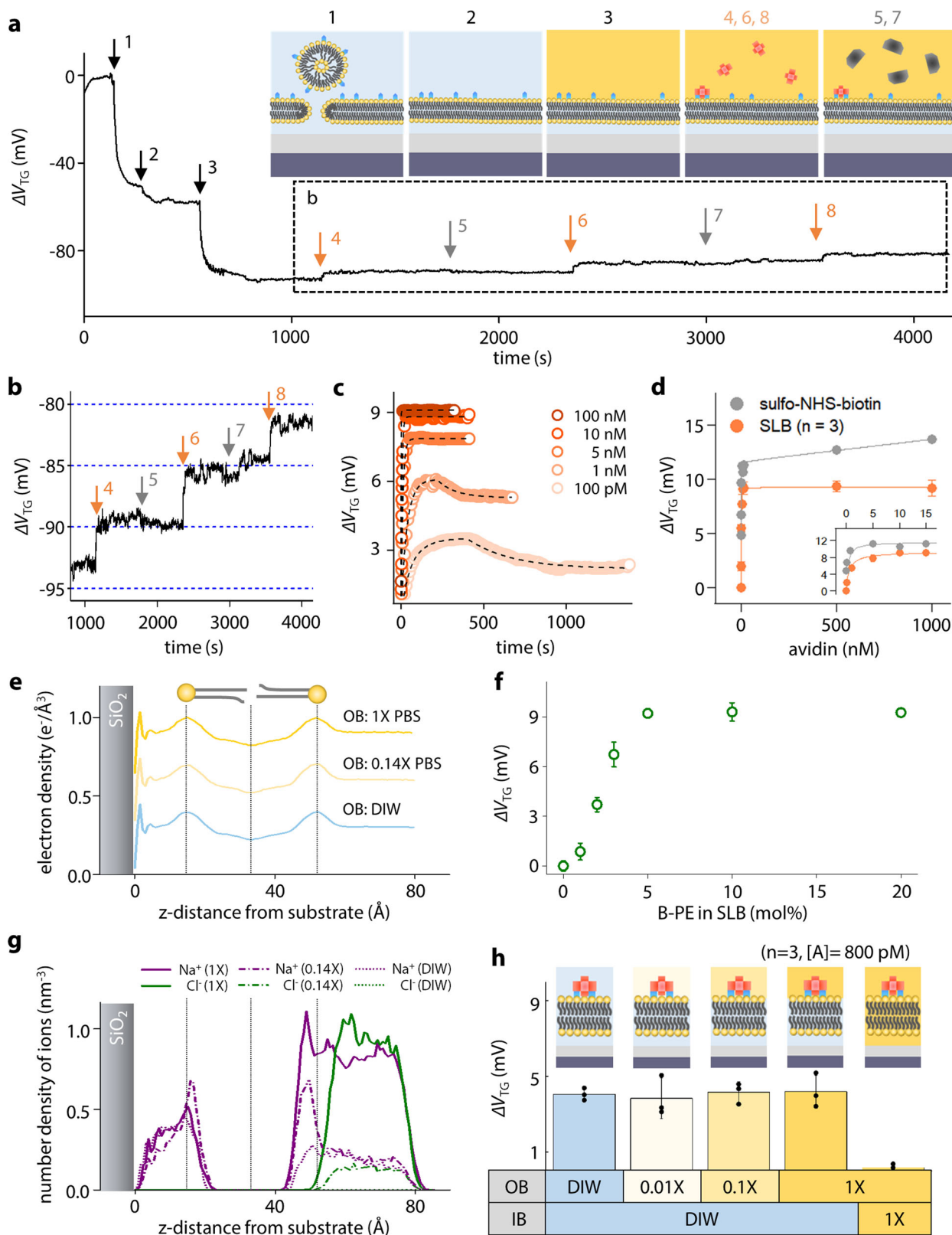


Fig. 2 SLB formation and its time-dependent measurement. **a** Schematic illustration of SLB formation. **b** Real-time tracing during an SUV rupture process. Insets show fluorescent images of the EG after SLB formation at different vesicle concentrations; (marker 1) after O_2 plasma treatment, (marker 2) at $1 \mu\text{g mL}^{-1}$, and (marker 6) at $5 \mu\text{g mL}^{-1}$. **c** I_D - V_{BG} curves with different ingredients in the SLB. **d** Time-dependent FRAP measurement. The scale bar in the inset is $50 \mu\text{m}$. Source data are provided as a Source Data file.



The real-time responses of biotin–avidin bindings at different analyte concentrations ranging from 100 pM to 100 nM are shown in Fig. 3c and summarized in Fig. 3d. To account for the obtained responses, an analytical model was suggested by combining the Langmuir isotherm model with the information of capacitively induced charges on the gate electrode of the FET.

The induced voltage change ΔV_{TG} can be described as

$$\Delta V_{TG}([A]) = \frac{q_A}{C_{TG}} [B]_{\max} \frac{[A]}{[A] + K_{eq}} \tag{1}$$

where q_A is the effective charge induced by molecular adsorption, $[B]_{\max}$ is the number of binding sites on the lipid membrane, $[A]$

Fig. 3 Measurements of biotin-avidin bindings using SLB-FET. **a** Real-time measurement for SLB formation and sequential molecular bindings. The inset illustrates different measurement stages. **b** Enlarged graph in **a** showing binding selectivity to avidin. **c** Real-time traces (circle) from biotin-avidin binding at different concentrations. Dashed lines represent fits by an analytical model. **d** Response amplitudes as a function of avidin concentration in the presence (orange)/absence (gray) of the SLB. The reported values of the SLB experiment represent the mean \pm standard deviation (SD) for $n = 3$ independent experiments. **e** Electron density profile of supported lipid bilayer with different OB ionic concentrations obtained from the MD simulation. **f** ΔV_{TG} at different concentrations of B-PE expression in the SLB with the constant number of avidin binders. The reported values of the SLB experiment represent the mean \pm standard deviation (SD) for $n = 3$ independent experiments. **g** MD simulation results of ion distribution of (Na^+ and Cl^-) at different concentrations. Note that significant Na^+ peaks at $z = 10$ and 50 \AA results from the lipid head group of the B-PE. **h** Sensor responses to 800 pM -avidin under different ionic conditions around the SLB. The measurement was performed for $n = 3$ independent experiments and all reported values represent the mean \pm SD. Source data are provided as a Source Data file.

represents the analyte concentration, and K_{eq} is the equilibrium constant²². The K_{eq} of 621.9 pM for biotin-avidin binding was determined from the fitting using Eq. (1) (solid line in orange, Fig. 3d), which is consistent with the literature^{19,23}. To determine binding parameters, a resistor-capacitor (RC) circuit model was combined with the first order Langmuir adsorption equation (see Supplementary Note 7 for details). The time-dependent ΔV_{TG} is then expressed as

$$\Delta V_{TG}(t) = \begin{cases} \frac{q_A}{C_{TG}} [B]_{\max} \left(1 - e^{-(k_1[A] + k_{-1})t}\right) + V_p(1 - e^{-\frac{t}{\tau_1}}) & t < T \\ \frac{q_A}{C_{TG}} [B]_{\max} \left(1 - e^{-(k_1[A] + k_{-1})t}\right) + V_p e^{-\frac{t}{\tau_2}} & t \geq T \end{cases} \quad (2)$$

where k_1 and k_{-1} are the association and dissociation rate constants, respectively, V_p is the difference between the maximum sensor response ($q_A[B]_{\max}/C_{TG}$) and the maximum value of $\Delta V_{TG}(t)$, and τ_1 and τ_2 are the RC time constants. The rate constants were calculated to be $k_1 = 1.64 \pm 0.06 \times 10^7 \text{ M}^{-1} \text{ s}^{-1}$ and $k_{-1} = 1.02 \times 10^{-2} \text{ s}^{-1}$ based on fitting with the obtained value of K_{eq} ($=k_{-1}/k_1$) above (Fig. 3c). The response curve from the EG functionalized by biotin at an identical concentration without the SLB (circle in gray, Fig. 3d) shows a linear increase in the high concentration regime, which is attributable to the non-specific binding²⁴. In contrast, this non-specific binding behavior was strongly suppressed by the SLB (Fig. 3d orange, and Fig. 3f). We conducted molecular dynamics (MD) simulation to investigate the possibility of conformational change in the SLB under different OB conditions (Fig. 3e, g). From Fig. 3e, we concluded that the SLB preserved its structure under different ionic strengths. In addition, titrations of avidin at a fixed concentration (10 nM) to the gradually increased B-PE concentration ($0, 1, 2, 3, 5, 10,$ and $20 \text{ mol}\%$) were tested out in identical buffer conditions (IB for DIW, and OB for $1 \times \text{PBS}$). A drastic increase of the ΔV_{TG} with respect to the B-PE concentrations ($0 \rightarrow 5 \text{ mol}\%$) was observed. The saturated amplitude of $\Delta V_{TG} \approx 9.3 \text{ mV}$ at higher concentrations was well agreed with the results shown in Fig. 3d. From those, we confirmed that the SLB plays essential roles not only as a “protector” against charge-assisted binders including non-specific bindings, but also as an “ion keeper” enabling reliable signal acquisition under ionic outer buffer solution.

Figure 3h presents the sensor responses using different conditions for the buffer solution (OB: DIW, $0.01 \times$, $0.1 \times$, and $1 \times \text{PBS}$, IB: DIW, and $1 \times \text{PBS}$) around the SLB. Unlike the usual presumption that the sensing capability highly depends on the ionic strength of the solution, the responses to 800 pM avidin in different buffer conditions were measured alike within the error range. The control experiment with $1 \times \text{PBS}$ buffer solution underneath the SLB inevitably demonstrates the importance of the ionic condition of the inner buffer (IB) in our SLB-FET sensing mechanism. In addition, $[B]_{\max}$ and C_{TG} are calculated to be 1.74×10^8 and 0.37 pF respectively in $5 \text{ mol}\%$ of the B-PE. With this, q_A is obtained to be $2.59 \times 10^{-23} \text{ C}$ ($\approx 1.61 \times 10^{-4}$

electrons) from the fitting. This suggests a significant discrepancy with the previous result of about 3.43 electrons for a single avidin molecule in $1 \times \text{PBS}$ solution²⁵. These counter-intuitive results exhibiting ionic strength-independent FET signals led us to the following hypothesis: there could be a possible conformational change upon molecular binding, redistributing the electron density within the SLB.

Analysis on the electron density change in the SLB upon molecular bindings. To investigate the underlying sensing mechanism of our SLB-FET upon molecular binding, synchrotron X-ray reflectometry (XRR) was applied to acquire electron density profiles across the SLB (DOPC/B-PE = $95/5$ in DIW) before/after avidin bindings²⁶. The obtained electron density profiles from the reflectivity fits are presented in Fig. 4a (see Supplementary Fig. 9b for details). Despite the structural similarity, conformational changes to the free-standing SLB due to avidin binding are distinguishable, and are accompanied by the redistribution of electrons within the SLB. For quantitative analysis, differences in the electric field (ΔE) and chemical potential ($\Delta\psi$) were calculated using Poisson’s equation (see Supplementary Note 9 for details) (Fig. 4b, c, and d). The induced chemical potential difference, $\Delta\psi$, via the avidin binding was 697 mV from XRR and 499 mV from MD simulation at the surface of the SiO_2 layer (Fig. 4d, f). Considering a series of potential drops along the circuit (Fig. 1g), the potential change at the top gate was calculated to be 12.2 and 8.73 mV respectively. This is consistent with the experimentally measured value, $q_A[B]_{\max}/C_{TG}$ of $9.38 \pm 3.08 \text{ mV}$ in the FET, considering the fact that the XRR experiment was conducted under DIW conditions ($\text{EDL}_{\text{DIW}} \gg \text{EDL}_{1 \times \text{PBS}}$). Note that the ΔV_{TG} caused by the charges above the SLB ($>55 \text{ \AA}$ in Fig. 4b) is within the range of standard deviation in the FET measurements. To further cement our understanding, we compared the signal responses of avidin variants (neutrAvidin: pI. 6.3 , streptavidin: pI. $5-6$, and avidin: pI. 10.5) with different isoelectric points (pIs) under $1 \times \text{PBS}$ at the identical concentration of 800 pM (Fig. 4g). Coterminous FET responses regardless of different pIs support our finding that the majority of effective signals originate from dipole field change within the SLB (see Supplementary Note 11 for details), not from the conjugated proteins themselves²⁷.

Discussion

Most hitherto electrical sensing of molecules required buffer dilution to weaken the ionic strength of solutions. However, the structural integrity and molecular activity of target analytes are not guaranteed in such attenuated ionic environments. Previous experiments with the SLB over probing materials showed an inevitable loss of sensitivity due to the screening effect by ion accumulation between the probing surface and SLB. Meanwhile, by placing DIW underneath the SLB, we successively traced potentiometric change by the SLB formation (Fig. 2b), as well as

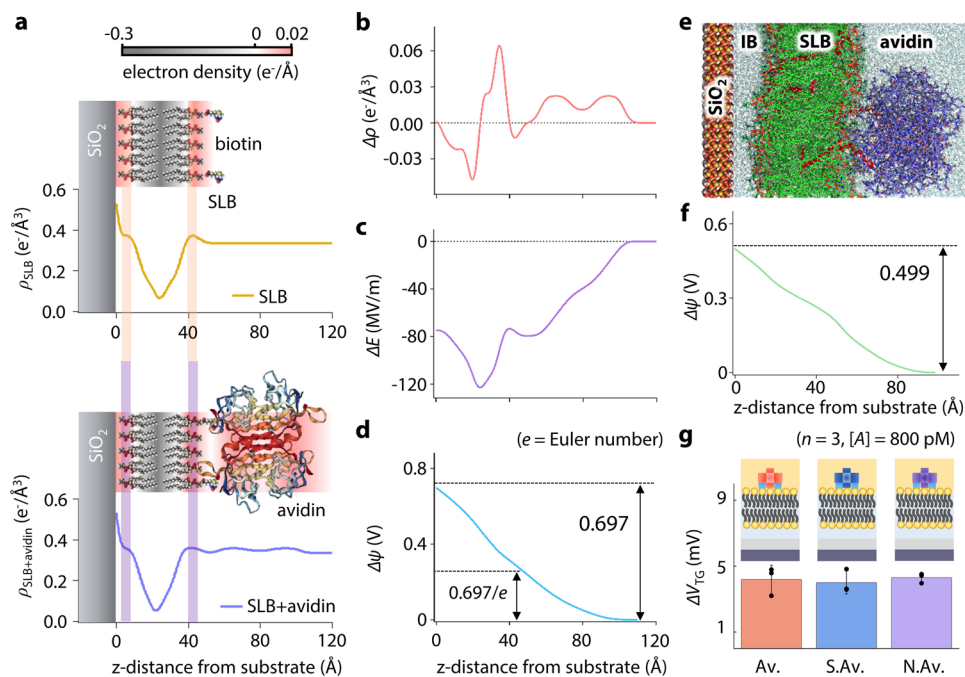


Fig. 4 Redistribution of the electron density in the SLB upon biotin-avidin bindings. **a** Electron density profiles before and after biotin-avidin bindings. **b** Electron density difference ($\Delta\rho = \rho_{\text{SLB+avidin}} - \rho_{\text{SLB}}$). **c** Electric field change. **d** Chemical potential difference upon biotin-avidin binding. **e** MD simulation of the SLB under avidin binding. The DOPC lipids, B-PE lipids, avidin, and water molecules are colored in green, red, purple, and cyan, respectively. **f** Induced potential difference upon biotin-avidin binding obtained from MD simulation (see Supplementary Note 11 for details). **g** Sensor responses to different analytes at identical concentrations. (Av. avidin, S.Av. streptavidin, and N.Av. neutrAvidin). The measurement values represent the mean \pm SD for $n = 3$ independent experiments. Source data are provided as a Source Data file.

Table 1 Comparison of FET sensors for molecule detection.

SLB?	Electron channel	Analyte	LOD	Solvent type & conc.	Refs.
○	Si	Av, S.Av, N.Av	100 pM	1× (100 mM) PBS	Our work
○	CNT	S.Av	2.5 μM	10 mM PBS	46
○	CNT	S.Av	5 μM	1 μM PBS	47
○	OSC	S.Av	10 nM	10 mM PBS	48
○	Graphene	Magainin 2	100 pM	10 mM NaF	27
○	Graphene	CTxB	12.5 nM	10 mM HEPES	49
×	Si	PSA	75 fg mL^{-1}	1 mM PBS, 2 mM KCl	50
×	Si	Thrombin	330 pM	Acetate buffer	51
×	Si	PSA	150 fM	100 μM PBS, 100 μM KCl	52
×	Si	cTnT	1 fg mL^{-1}	100 μM PBS	53
×	Si	PSA	1 pg mL^{-1}	1 μM PBS, 2 μM KCl	54

LOD limit of detection, Av Avidin, S.Av Streptavidin, N.Av NeutrAvidin, OSC organic semiconductor, PSA Prostate-specific antigen, cTnT Cardiac troponin T.

protein bindings above the SLB to the “world’s lowest level of the limit of detection (LOD)” in physiologic conditions of 1× PBS with the SLB (Table 1). The exceptional capabilities of this SLB-FET are attributed to the following elements: (i) defect-free coverage of lipid membrane, (ii) directional alignment of receptors, (iii) prohibition of non-specific binders on the SLB, and most importantly, (iv) ion impermeability of the SLB. Note that the combination of all the ingredients described above resulted in the realization of reliable signal acquisition in solution at physiological ionic strength via the extension of the effective detection range (=Debye length extension) with the vertical shift of stern- and diffusive-layers (Fig. 5). We found that placing the DIW underneath the SLB is the key for shifting the EDL above the outmost surface of the SLB, translating the lipid membrane into a faultless transducer (Fig. 3h). X-ray reflectometry and the corresponding equivalent circuit analysis clearly explained the origin of the obtained electrical responses and their signal transfer

mechanism via sub-nanoscale conformational change of lipids during binding events, which were independent from the ionic strengths of the outer buffer solution and even the effective charge states of the bound molecules (Figs. 3h and 4g). In particular, striking FET responses with coterminous amplitudes upon protein bindings with distinct pIs obviously support our findings on the sensing mechanism. Note here that this sensing mechanism by the conformational change in the SLB allows for the detection of electroneutral targets. To the best of our knowledge, our SLB-FET platform presents the first experimental observation of the SLB conformational changes upon molecular binding events with an in-vitro electrical detector, which has been long proposed as a theory but was never experimentally validated. This opens up an opportunity to analyze the physicochemical modulation of lipids at the molecular level, ruling out any possible contribution of the effective charge of target proteins in the signal-transducing mechanism. By resolving the chronic concern

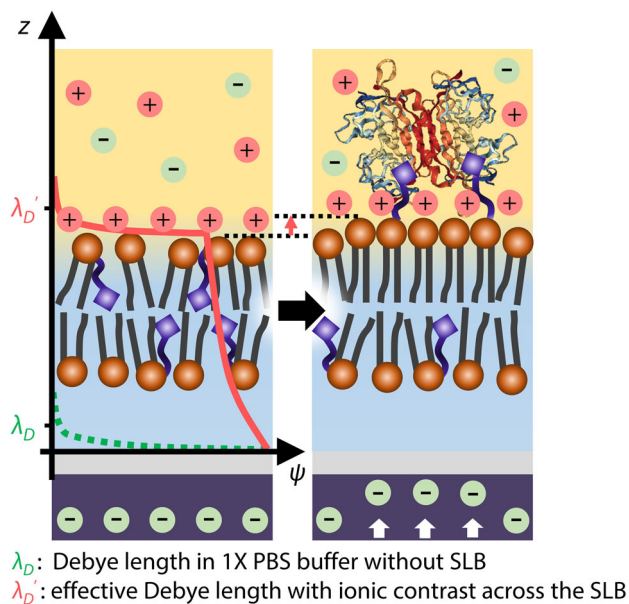


Fig. 5 Improved molecular detection via asymmetric ionic environment across the SLB. Schematic illustration of effective Debye length (λ_D') with ionic contrast across the SLB and conformational change upon avidin binding.

of molecular detection in physiologically relevant conditions, our SLB-FET platform and resultant exceptional performance can be extended to identify essential roles of membrane-related pathogenic proteins, and stages/factors of diseases and apoptosis of cells that experience lipid membrane rupture processes. This has wide-ranging implications for conditions such as neurodegenerative disorders, including Alzheimer's and Parkinson's diseases^{28,29}, virus-cell membrane interaction^{30,31}, and the impact of micro-particles on the human respiratory system³².

Methods

Fully depleted silicon-on-insulator device fabrication process. Conventional fabrication processes were conducted to construct FET devices, known as Si-nanoribbons²² (Supplementary Fig. 1). SIMOX-SOI wafers (100 nm-thick top-Si, Shinetsu) were used to enable top and bottom gating with high precision. In step 1, we selectively etched the top-Si layer using a reactive ion etching (RIE) process to define the active current channel (5 μm long and 30 μm wide) in the FET. A 15-nm-thick oxide layer was formed over the entire top-Si surface using a dry oxidation process (step 2), and confirmed by transmission electron microscope (TEM, Tecnai F20 G2, FEI). For the top gate (TG) electrode, a 200-nm-thick polysilicon (poly-Si) film was deposited, followed by selective etching of the poly-Si and SiO₂ layers (steps 3 and 4). To minimize the Schottky barrier in metal contacts, arsenic (As) implantation (step 5) followed by annealing (step 6, 850 °C for 30 s) was performed. Then, Ti/TiN/Al/TiN (50/50/250/50 nm) layers were selectively etched using the RIE process, providing soldering pads (steps 7 and 8). Finally, we encapsulated the fabricated devices and mounted them on a printed circuit board with a pin-type interface.

Faraday shielding box and EG connections. The EG with the reaction chamber was placed in a metallic box for noise shielding. We applied the source and back-gate bias voltages (V_S and V_{BG}) with DC voltage sources (GS210, Yokogawa, Japan) with high precision and measured the drain current (I_D) with a digital multimeter (34410A, Agilent, USA). The EG was electrically wired to the TG and terminated with an Ag/AgCl reference electrode (LF-2, Innovative Instruments, Inc., USA) (Supplementary Fig. 2).

Vesicle preparation and SLB formation. The 1,2-dioleoyl-*sn*-glycero-3-phosphocholine (DOPC; base lipid of the SLB, molecular weight (MW) = 786.1 g mol⁻¹) and 1,2-dioleoyl-*sn*-glycero-3-phosphoethanolamine-*N*-(cap biotinyl) (B-PE, MW = 1105.5 g mol⁻¹) were purchased from Avanti Polar Lipids Inc. Texas Red 1,2-dihexadecanoyl-*sn*-glycero-3-phosphoethanolamine (TR-DHPE, MW = 1381.85 g mol⁻¹) was purchased from Life Technologies, Carlsbad, CA. Avidin variants (avidin,

streptavidin, and neutrAvidin, MW = 68, 53, and 60 kDa each.) and various concentrations of PBS solutions were purchased from ThermoFisher Scientific. The SLB membrane consists of 95 mol% DOPC and 5% B-PE (receptor of avidin variants). For vesicle preparation, we used the rapid solvent exchange method to evaporate chloroform and hydrate with buffer solution (DIW or 1× PBS) simultaneously²⁰. After that, the prepared vesicle solutions were extruded 20 times through 50-nm-diameter pores (PC membrane, Avanti Polar Lipids Inc., USA) to prepare uniformly sized, small unilamellar vesicles (SUV; 0.1 mg mL⁻¹). The 50-nm-diameter SUVs spontaneously rupture on a hydrophilic SiO₂ surface and form a uniform and defect-free SLB patch on the SiO₂ surface of the EG^{33,34}. For negative controls for biotin-avidin binding, Cholera toxin subunit B proteins (CTxB, Invitrogen, USA, MW = 12 kDa) specifically bound to ganglioside GM1 lipids were used.

Measurement setup for X-ray reflectivity (XRR). Synchrotron XRR measurement was carried out using the beamline 5 A, MS-XRS (16.2 keV) in the Pohang Accelerator Laboratory (PAL) with a customized liquid cell. The aluminum liquid cell has Kepton-sealed windows, which are transparent to synchrotron X-ray wavelength, allowing X-ray to be reflected from the surface of the sample while maintaining an aqueous environment inside (Supplementary Fig. 6). The cross-sectional beam size of incident X-ray was 500 × 400 μm^2 , which is large enough to ensure the averaging effect³⁵. The SLB (DOPC:B-PE = 95:5) in the DIW was formed via the vesicle fusion method on the 300 nm-thick SiO₂-coated Si wafer and annealed at 40 °C for 30 min. We injected 800 pM-avidin solution into the SLB and waited for another 30 min to reach equilibrium in the biotin-avidin reaction. After washing to remove protein residues, the wafer was mounted in the liquid cell (Supplementary Fig. 6), which is filled with DIW before the XRR measurement.

Electron density profile in the SLB obtained from X-ray reflectivity measurement. We used the slab model based on Parratt's method³⁶ (Supplementary Fig. 9) combined with a genetic algorithm to calculate reflectivity. We modeled the SLB with five slabs: two lipid head groups, two lipid tail layers, and a single empty space between each leaflet. For avidin adsorption, four additional slabs were used: three layers of protein and a single layer of DIW between the avidin and the bilayer surfaces. The roughness between each slab was assumed to be 3 Å. Unlike the conventional SLB electron density fitting in which the symmetric electron density profile is assumed, we supposed an asymmetric structure considering that the lipid head group and tail layer in the upper leaflet and bottom leaflet can have different electron densities via avidin adsorption.

System parameters for all-atom molecular dynamics (AA MD) simulations. We conducted all-atom molecular dynamics simulations in GROMACS 5.1.4³⁷ using the CHARMM36 force-field³⁸. A leapfrog integrator with a time-step of 2 fs was used for all simulations, restraining all bonds with the LINCS algorithm³⁹. The electrostatic interactions of the system were calculated based on the PME with a cutoff of 1.2 nm. Neighbor lists were built using the Verlet cutoff scheme with a cutoff range of 1.2 nm and were updated at every step of the simulations. The temperature was controlled at 298.15 K by a V-rescale thermostat⁴⁰. All systems were maintained at 1 bar using the Berendsen⁴¹ and Parrinello-Rahman⁴² for the equilibrium and production run, respectively.

AA MD simulations for SLB on SiO₂ surface with ionic contrast. We built a binary bilayer made up of DOPC (95%) and B-PE (5%) via the CHARMM-GUI⁴³ membrane builder. Ionic contrast between outer buffer and inner buffer can be generated during MD by inserting a SiO₂ surface. We set up 3 simulation systems with ionic contrast and 1 simulation system without ionic contrast. Overall charge neutrality for all systems was achieved by adding the counter ions. Periodic boundary conditions were applied to x , y , and z directions with an initial cell size of 7.5 × 7.5 × 8 nm³. After 100 ns equilibrium steps with pressure coupling, the production simulations were performed for 100 ns to calculate the electron density profile. The electron density profiles of SLB were calculated at the final 10 ns trajectory by the GROMACS analysis tool.

AA MD for electron redistribution of SLB after avidin binding. The initial structure of the avidin was obtained from the Protein Data Bank (PDB), named 2AVI⁴⁴. For analyzing the electron redistribution after avidin binding, we built the avidin bound binary bilayer system with DOPC/B-PE and the system with DPPC/B-PE. Periodic boundary conditions were applied to x , y , and z directions with an initial cell size of 10 × 10 × 14 nm³ and 9 × 9 × 20 nm³, respectively. We conducted 400 ns simulations for the equilibration of the structure and 100 ns simulations for analysis. The electron density profiles and dipole potential of avidin bound SLB were calculated by the GROMACS analysis tool. The APL@Voro program⁴⁵ generating the Voronoi diagrams was used for Voronoi analysis and calculation of area per lipids.

Data availability

All relevant data are available from the authors upon reasonable request. Source data are provided with this paper.

Received: 22 October 2020; Accepted: 3 June 2021;

Published online: 18 June 2021

References

- Mabeck, J. T. & Malliaras, G. G. Chemical and biological sensors based on organic thin-film transistors. *Anal. Bioanal. Chem.* **384**, 343–353 (2006).
- Schoning, M. J. & Poghossian, A. Recent advances in biologically sensitive field-effect transistors (BioFETs). *Analyst* **127**, 1137–1151 (2002).
- Thompson, L. A., Kowalik, J., Josowicz, M. & Janata, J. Label-free DNA hybridization probe based on a conducting polymer. *J. Am. Chem. Soc.* **125**, 324–325 (2003).
- Bunimovich, Y. L. et al. Quantitative real-time measurements of DNA hybridization with alkylated nonoxidized silicon nanowires in electrolyte solution. *J. Am. Chem. Soc.* **128**, 16323–16331 (2006).
- Jiang, Y. W. & Tian, B. Z. Inorganic semiconductor biointerfaces. *Nat. Rev. Mater.* **3**, 473–490 (2018).
- Ji, T. et al. Detection of COVID-19: A review of the current literature and future perspectives. *Biosens. Bioelectron.* **166**, 112455 (2020).
- Park, J. K. & Cho, W. J. Development of high-performance fully depleted silicon-on-insulator based extended-gate field-effect transistor using the parasitic bipolar junction transistor effect. *Appl. Phys. Lett.* **101**, 133703 (2012).
- Spijkman, M. J. et al. Dual-gate thin-film transistors, integrated circuits and sensors. *Adv. Mater.* **23**, 3231–3242 (2011).
- Huang, W., Diallo, A. K., Dailey, J. L., Besar, K. & Katz, H. E. Electrochemical processes and mechanistic aspects of field-effect sensors for biomolecules. *J. Mater. Chem. C* **3**, 6445–6470 (2015).
- Gao, N. et al. Specific detection of biomolecules in physiological solutions using graphene transistor biosensors. *Proc. Natl Acad. Sci. USA* **113**, 14633–14638 (2016).
- Kulkarni, G. S., Reddy, K., Zhong, Z. H. & Fan, X. D. Graphene nanoelectronic heterodyne sensor for rapid and sensitive vapour detection. *Nat. Commun.* **5**, 4376 (2014).
- Elnathan, R. et al. Biorecognition layer engineering: overcoming screening limitations of nanowire-based FET devices. *Nano Lett.* **12**, 5245 (2012).
- Nakatsuka, N. et al. Aptamer-field-effect transistors overcome Debye length limitations for small-molecule sensing. *Science* **362**, 319–324 (2018).
- del Castillo, J., Rodriguez, A., Romero, C. A. & Sanchez, V. Lipid films as transducers for detection of antigen-antibody and enzyme-substrate reactions. *Science* **153**, 185–188 (1966).
- Tabaei, S. R., Ng, W. B., Cho, S. J. & Cho, N. J. Controlling the formation of phospholipid monolayer, bilayer, and intact vesicle layer on graphene. *ACS Appl. Mater. Interfaces* **8**, 11875–11880 (2016).
- Poyry, S. & Vattulainen, I. Role of charged lipids in membrane structures - Insight given by simulations. *Biochim. Biophys. Acta* **1858**, 2322–2333 (2016).
- Spijkman, M. J. et al. Beyond the Nernst-limit with dual-gate ZnO ion-sensitive field-effect transistors. *Appl. Phys. Lett.* **98**, 043502 (2011).
- Han, X. J. et al. Manipulation and charge determination of proteins in photopatterned solid supported bilayers. *Integr. Biol.* **1**, 205–211 (2009).
- Liu, Z. et al. Specific binding of avidin to biotin-containing lipid lamella surfaces studied with monolayers and liposomes. *Eur. Biophys. J.* **24**, 31–38 (1995).
- Ryu, Y. S. et al. Reconstituting ring-rafts in bud-mimicking topography of model membranes. *Nat. Commun.* **5**, 4507 (2014).
- Ryu, Y. S. et al. Lipid membrane deformation accompanied by disk-to-ring shape transition of cholesterol-rich domains. *J. Am. Chem. Soc.* **137**, 8692–8695 (2015).
- Duan, X. et al. Quantification of the affinities and kinetics of protein interactions using silicon nanowire biosensors. *Nat. Nanotechnol.* **7**, 401–407 (2012).
- Kohanski, R. A. & Lane, M. D. Monovalent avidin affinity columns. *Methods Enzymol.* **184**, 194–200 (1990).
- Maletinska, L. et al. Human glioblastoma cell lines: Levels of low-density lipoprotein receptor and low-density lipoprotein receptor-related protein. *Cancer Res.* **60**, 2300–2303 (2000).
- Hideshima, S., Nakamura, T., Kuroiwa, S. & Osaka, T. Relation between effective charge numbers and signals caused by protein adsorption on field effect transistor detection. *ECS Trans.* **35**, 121–124 (2011).
- Horton, M. R., Reich, C., Gast, A. P., Radler, J. O. & Nickel, B. Structure and dynamics of crystalline protein layers bound to supported lipid bilayers. *Langmuir* **23**, 6263–6269 (2007).
- Ang, P. K. et al. A Bioelectronic platform using a graphene-lipid bilayer interface. *ACS Nano* **4**, 7387–7394 (2010).
- Fabiani, C. & Antollini, S. S. Alzheimer's disease as a membrane disorder: spatial cross-talk among beta-amyloid peptides, nicotinic acetylcholine receptors and lipid rafts. *Front. Cell Neurosci.* **13**, 309 (2019).
- Shahmoradian, S. H. et al. Lewy pathology in Parkinson's disease consists of crowded organelles and lipid membranes. *Nat. Neurosci.* **22**, 1099–1109 (2019).
- Basso, L. G. M., Vicente, E. F., Crusca, E., Cilli, E. M. & Costa, A. J. SARS-CoV fusion peptides induce membrane surface ordering and curvature. *Sci. Rep.* **6**, 37131 (2016).
- Stadler, K. et al. SARS—beginning to understand a new virus. *Nat. Rev. Microbiol.* **1**, 209–218 (2003).
- Xing, Y. F., Xu, Y. H., Shi, M. H. & Lian, Y. X. The impact of PM2.5 on the human respiratory system. *J. Thorac. Dis.* **8**, E69–E74 (2016).
- Ryu, Y. S. et al. Continuity of monolayer-bilayer junctions for localization of lipid raft microdomains in model membranes. *Sci. Rep.* **6**, 26823 (2016).
- Baek, J. M. & Ryu, Y. S. Surface sensitive analysis device using model membrane and challenges for biosensor-chip. *Biochip J.* **14**, 110–123 (2020).
- Lee, S., Jeong, D. W. & Choi, M. C. Vertical order of DPPC multilayer enhanced by cholesterol-induced ripple-to-liquid ordered (LO) phase transition: synchrotron X-ray reflectivity study. *Curr. Appl. Phys.* **17**, 392–397 (2017).
- Parratt, L. G. Surface studies of solids by total reflection of X-rays. *Phys. Rev.* **95**, 359–369 (1954).
- Abraham, M. J., Murtola, T., Schulz, R., Páll, S., Smith, J. C., Hess, B. & Lindahl, E. GROMACS: high performance molecular simulations through multi-level parallelism from laptops to supercomputers. *SoftwareX* **1**, 19–25 (2015).
- Klauda, J. B. et al. Update of the CHARMM all-atom additive force field for lipids: validation on six lipid types. *J. Phys. Chem. B* **114**, 7830–7843 (2010).
- Hess, B., Bekker, H., Berendsen, H. J. C. & Fraaije, J. G. E. M. LINC: a linear constraint solver for molecular simulations. *J. Comput. Chem.* **18**, 1463–1472 (1997).
- Bussi, G., Donadio, D. & Parrinello, M. Canonical sampling through velocity rescaling. *J. Chem. Phys.* **126**, 01410 (2007).
- Berendsen, H. J., Postma, J. V., van Gunsteren, W. F., DiNola, A. & Haak, J. Molecular dynamics with coupling to an external bath. *J. Chem. Phys.* **81**, 3684–3690 (1984).
- Parrinello, M. & Rahman, A. Polymorphic transitions in single crystals: a new molecular dynamics method. *J. Apply. Phys.* **52**, 7182–7190 (1981).
- Jo, S., Kim, T., Iyer, V. G. & Im, W. CHARMM-GUI: a web-based graphical user interface for CHARMM. *J. Comput. Chem.* **29**, 4486–4494 (2008).
- Livnah, O., Bayer, E. A., Wilchek, M. & Sussman, J. L. Three-dimensional structures of avidin and the avidin-biotin complex. *Proc. Natl Acad. Sci. USA* **90**, 5076–5080 (1993).
- Lukat, G., Krüger, J. & Sommer, B. APL@Voro: a Voronoi-based membrane analysis tool for GROMACS trajectories. *J. Chem. Inf. Model.* **53**, 2908–2925 (2013).
- Star, A., Gabriel, J. C. P., Bradley, K. & Gruner, G. Electronic detection of specific protein binding using nanotube FET devices. *Nano Lett.* **3**, 459–463 (2003).
- Zhou, X. J., Moran-Mirabal, J. M., Craighead, H. G. & McEuen, P. L. Supported lipid bilayer/carbon nanotube hybrids. *Nat. Nanotechnol.* **2**, 185–190 (2007).
- Magliulo, M. et al. Electrolyte-gated organic field-effect transistor sensors based on supported biotinylated phospholipid bilayer. *Adv. Mater.* **25**, 2090–2094 (2013).
- Kuo, C. J. et al. Lipid-modified graphene-transistor biosensor for monitoring amyloid-beta aggregation. *ACS Appl. Mater. Inter.* **10**, 12311–12316 (2018).
- Zheng, G. F., Patolsky, F., Cui, Y., Wang, W. U. & Lieber, C. M. Multiplexed electrical detection of cancer markers with nanowire sensor arrays. *Nat. Biotechnol.* **23**, 1294–1301 (2005).
- Kim, K. S., Lee, H. S., Yang, J. A., Jo, M. H. & Hahn, S. K. The fabrication, characterization and application of aptamer-functionalized Si-nanowire FET biosensors. *Nanotechnology* **20**, 235501 (2009).
- Zheng, G. F., Gao, X. P. A. & Lieber, C. M. Frequency domain detection of biomolecules using silicon nanowire biosensors. *Nano Lett.* **10**, 3179–3183 (2010).
- Chua, J. H., Chee, R. E., Agarwal, A., Wong, S. M. & Zhang, G. J. Label-free electrical detection of cardiac biomarker with complementary metal-oxide semiconductor-compatible silicon nanowire sensor arrays. *Anal. Chem.* **81**, 6266–6271 (2009).
- Kim, A. et al. Ultrasensitive, label-free, and real-time immunodetection using silicon field-effect transistors. *Appl. Phys. Lett.* **91**, 103901 (2007).

Acknowledgements

This work was supported by KIST Institutional Programs (Nos. 2E31253, 2E31251, and 2E31271) and the Joint research lab program of the National Agenda research division, KIST. The National Research Foundation of Korea (NRF) grant funded by the Korea government (MSIT) (Nos. 2020R1A2C2005486, 2018R1A2B3001690, 2021R1A2C2009236, and 2017M3D1A1039421).

Author contributions

D.L., Y.-S.R., and C.K. designed the experiments, analyzed the data, and prepared the initial draft of the manuscript. D.L. fabricated FET devices and performed SLB-FET measurements. D.L., S.L., and M.C.C. conducted XRR experiments and analysis. E.-S.Y. obtained the fluorescence microscopy images and performed the FRAP experiment. E.-S.Y., H.S.S., J.H.K., and K.H.L. prepared SLBs and test analytes and provided technical assistance in handling samples. S.L., T.L., and S.-K.H. conducted electrical signal data analysis. W.H.J. and D.J.A. conducted MD simulations and analyses on ionic contrast phenomenon across the lipid membranes. All authors agreed on the final content.

Competing interests

The authors declare no competing interests.

Additional information

Supplementary information The online version contains supplementary material available at <https://doi.org/10.1038/s41467-021-24122-8>.

Correspondence and requests for materials should be addressed to D.J.A., Y.-S.R. or C.K.

Peer review information *Nature Communications* thanks the anonymous reviewers for their contribution to the peer review of this work.

Reprints and permission information is available at <http://www.nature.com/reprints>

Publisher's note Springer Nature remains neutral with regard to jurisdictional claims in published maps and institutional affiliations.



Open Access This article is licensed under a Creative Commons Attribution 4.0 International License, which permits use, sharing, adaptation, distribution and reproduction in any medium or format, as long as you give appropriate credit to the original author(s) and the source, provide a link to the Creative Commons license, and indicate if changes were made. The images or other third party material in this article are included in the article's Creative Commons license, unless indicated otherwise in a credit line to the material. If material is not included in the article's Creative Commons license and your intended use is not permitted by statutory regulation or exceeds the permitted use, you will need to obtain permission directly from the copyright holder. To view a copy of this license, visit <http://creativecommons.org/licenses/by/4.0/>.

© The Author(s) 2021